THE JOURNAL OF PHYSICAL CHEMISTRY C

Article

pubs.acs.org/JPCC

Core Dominated Surface Activity of Core–Shell Nanocatalysts on Methanol Electrooxidation

Tsan-Yao Chen,*[,†,‡] Tzy-Jiun Mark Luo,[‡] Yaw-Wen Yang,[§] Yu-Chen Wei,[∥] Kuan-Wen Wang,[∥] Tsang-Lang Lin,[†] Ten-Chin Wen,[⊥] and Chih Hao Lee[†,§]

[†]Department of Engineering and System Science, National Tsing Hua University, Hsinchu 30013, Taiwan

[‡]Department of Materials Science and Engineering, North Carolina State University, Raleigh, North Carolina 27695, United States

[§]National Synchrotron Radiation Research Center, Hsinchu 30076, Taiwan

[∥]Institute of Materials Science and Engineering, National Central University, Taoyuan 320, Taiwan

[⊥]Department of Chemical Engineering, National Cheng Kung University, Tainan 70001, Taiwan

Supporting Information

ABSTRACT: The activity of core–shell nanoparticles (NCs) in electrooxidation of methanol (MOR) was found to be dependent on the crystalline structure of the core and the lattice strain at the core–shell interface. Ru-core and Pt-shell NCs delivered 6.1-fold peak MOR current density at −135 mV than Pt NCs, while the Co-core and Pt-shell NCs showed a 1.4-fold peak MOR current density at 280 mV. The current density is improved by the compressive lattice strain of the surface that is caused by the lattice mismatch between the Pt shell and the Ru core. For Co-core NCs, the enhancement results from the ligand effect at surface Pt sites. In addition, the Ru-core NCs maintained a steady current density of 0.11 mA cm^{-2} at 500 mV in a half-cell system for 2 h, which is 100-fold higher than that of Pt NCs and Co-core NCs. These results provide mechanistic information for the development of fuel cell catalysts along with reduced Pt utilization and programmable electrochemical performance.

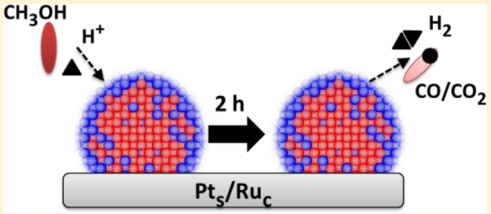

INTRODUCTION

The kinetic rate of catalytic reaction and its stability over time are the deciding factors for fuel cell performance. For example, the rate-determining step in direct-methanol fuel cells (DMFC) is methanol oxidation reaction (MOR), and therefore, a slow MOR such as slow dissociation of water and oxygen molecules is considered to be the main barrier to a better efficiency.[1,2] Because all platinum catalysts in DMFC are deposited as thin films on supporting substrates, the changes to the platinum crystal lattice at the interface also affect the efficiency of battery operation.[1,3] Therefore, core–shell architecture (i.e., bimetallic heterogeneous catalysts) is an easy approach to achieve the tuning of lattice strain by carefully selecting the core metal while maintaining high specific surface area (m^2/g) through the size of nanoparticles (NCs).[4] Such catalysts have several advantages that make them attractive, including high Pt utilization (up to 100%), high electrochemical durability (potential cycles $>10^5$)[5] and outstanding electrochemical activities (room temperature CO oxidation).[1,6,7] These effects are due to the modulation of d-band centriod caused by the lattice strain.[8] The effects of strain catalytic reaction can be simulated using density functional theory (DFT) using different configurations of model molecules on the surface. From heterogeneous catalysis point of view, the activity of NCs is mostly determined by the top three atomic layers of Pt atoms (about ∼4 Å depth).[4] However, the low electrochemical sustainability and the diffusion-limited bottleneck of the existing technology are still unable to achieve cost-effective and eco-friendly applications.

Our previous study focused on chemical composition and nanostructure of the outer shell.[9] Therefore, this paper focuses on how the structure of inner core affects the electrochemical property of the outer shell. Here we propose a new approach for synthesizing NCs[6,9] to achieve a better utilization of Pt and a stable and effective reaction by synthesizing NCs comprising of near-monolayer thick of Pt shell on different core crystallites NPs. In addition to the presence of the lattice strain, we also found that the formation of heterogeneous oxide layer also influence the surface activity. Such nanostructure may induce higher electronegativity and stronger chemisorptions of oxygen and hydroxide, consequently facilitating the electrooxidation of carbonaceous molecules.[10,11] In this paper, we will determine which mechanism (e.g., bifunctional effect, ligand effect, lattice strain, and surface atomic packing[1,3,4,12]) dominates the catalytic properties on each NCs and, more importantly, determine how to optimize the surface activities of bimetallic systems through the nanostructure.

Received: February 22, 2012
Revised: July 9, 2012
Published: July 15, 2012

dx.doi.org/10.1021/jp3017419 | J. Phys. Chem. C 2012, 116, 16969–16978

EXPERIMENTAL SECTION

In this paper, we synthesized the core−shell NCs with a Pt shell crystal in a thickness of near monolayer atoms by the sequentially designed polyol method combining with the seed mediated wet chemical reduction. To study how their surface activities been engineered by varying core crystallites, we utilized X-ray characterizations and electrochemical methods to depict the structure-to-activity correlations of core−shell NCs from microscopic to electronic standpoints. First, the nanoarchitecture of as synthesized NCs was confirmed by small-angle X-ray scattering (SAXS). The lattice strain in the shell region of these NCs affected by their structures of core crystallites was elucidated using X-ray diffraction (XRD). Meanwhile, the corresponding heteroatomic intermixes, chemical distributions, and unfilled valence orbital states (unfilled d states) of shell atoms were determined by X-ray absorption spectroscopy (XAS). Then, effects of core crystallites on binding energy and chemical distributions of surface shell atoms were illustrated by X-ray photoemission spectroscopy (XPS). Details of the experiments, characterizations, and discussions are given in the following and in Supporting Information (SI).

Synthesis of Core−Shell NCs with Monolayer Shell Crystallites. The core−shell NCs were synthesized by using two methods: the first method was applied to precisely grow the Pt shell on Ru core in near-atomic layer thick through a polyol reduction with a sequence controlling processes;[6,9] the second method enabled the deposition of Pt atoms on various metals or oxides.[13,14] The techniques used for growing Pt shell on Ru nanocrystallite were described in our previous works.[9] The Ru_{core}−Pt_{shell} NCs (denoted as Pt_s/Ru_c) has a Pt shell with a precisely controlled thickness around 1.5 atomic layers. The synthesis of Co_{core}−Pt_{shell} NCs (denoted as Pt_s/Co_c) was conducted by combining chemical reduction and poylol reaction. In the first step, cobalt core NPs was grown by wet chemical reduction method. It was conducted by adding 10 mL of 300 mM sodium borohydride [$NaBH_4$] water solution into 40 g of 20 mM cobalt acetate tetrahydrate [$C_4H_6CoO_4{\cdot}4H_2O$] ethylene glycol (EG) solution in a presence of 10 wt % of polyvinylpyrrolidone stabilizer (PVP-40, MW = 40 k). The solution of PVP blended Co NPs (Co-PVP) was redispersed in EG into a metal contain of 10 mM and then heated to 160 °C to dehydrate for 2 h. After dehydration and cooling to room temperature, the Pt shell crystal was grown by mixing Co-PVP with hexachloroplatinic acid [$H_2PtCl_6{\cdot}6H_2O$] in a Pt/Co ratio of 1 and then treated at 160 °C for another 2 h. The entire procedure was conducted under an ambient atmosphere.

NCs Characterizations. The crystal structure, local coordination environments, nanostructure, and chemical identities of core−shell NCs were respectively characterized by using XRD (with the incident X-ray wavelength of 1.3332 Å at the beamlines of BL-01C2, BL-07A of NSRRC in Taiwan, and BL-12B2 of SPring-8 in Japan), XAS (at beamlines of BL-17C and BL-01C1 of NSRRC, Taiwan), SAXS (at beamline of BL-23A of NSRRC, Taiwan), and XPS (beamline of BL-24A of NSRRC, Taiwan). The MOR activity of these NCs was monitored by using CV analysis (CH Instruments Model 600B). It was conducted in a homemade electrochemistry cell. The reference saturated calomel electrode (SCE, $Hg_2Cl_{2(s)}$/$Hg_{(l)}$) was employed to calibrate the potential of electrochemical reactions both at working anode and counter cathode (a standard foil of platinum, 10 × 10 mm^2). The working anode was prepared by spin coating the slurry of NCs on a commercial available fluorine-doped tin oxide (FTO) glass with a post heat treatment at 330 °C for 30 min under air atmosphere. The details of electrochemical experiments and X-ray characterizations are reported in the previous studies.[9]

RESULTS AND DISCUSSION

Nanostructure and Shell Thickness Determination. The nanostructures of as synthesized NPs are investigated using small-angle X-ray scattering analysis. Figure 1 shows the SAXS spectra [$I(q)$ vs q] of core−shell NCs that contains different core crystallites. As can be seen from the scattering

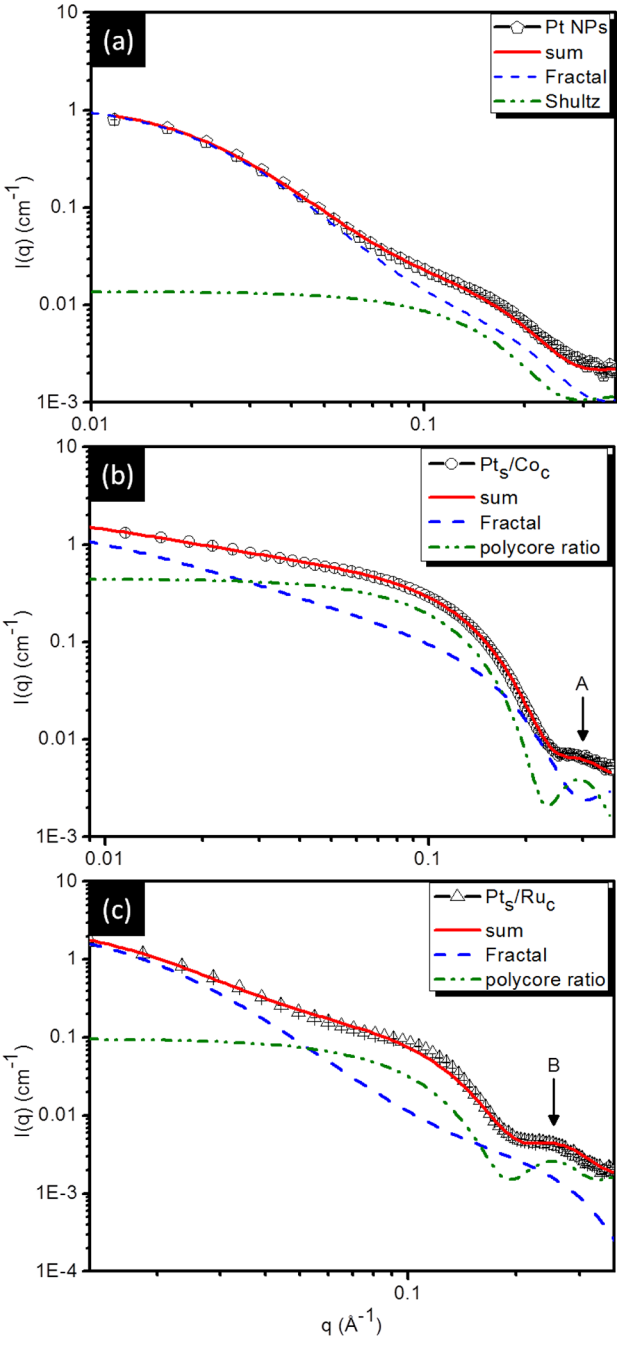

Figure 1. Small angle X-ray scattering spectra of as synthesized NCs, where arrows A and B denote the scattering hump of the core−shell structure in the high q range.

dx.doi.org/10.1021/jp3017419 | J. Phys. Chem. C 2012, 116, 16969−16978

interference in the range of $q < 0.08$ Å^{-1}, these polymer (PVP stabilizer, *N*-vinylpyrrolidone) blended NPs will form meso-scale-disordered fractal clusters via interacting with each other through a screened coulomb potential when suspended in aqueous solution.[15] Given that the surface catalytic activity of core−shell NCs is the major concern, only the intraparticle structure information, which corresponds to the scattering oscillation in the range $q > 0.08$ Å^{-1}, is discussed here. From Figure 1, the spectra of bimetallic NCs (Pt_s/Co_c and Pt_s/Ru_c), comprising scattering humps as denoted by arrows A and B with considerable intensity extending to the q range until 0.39 Å^{-1}, are typical SAXS feature of NPs with core−shell structure.[16,17] Such scattering periodicity is a result from mainly the resonance scattering correlation of electron distribution within surface layer and partially the in-phase correlation scattering of hard sphere surface electrons. The thickness of shell crystal is determined by resolving the SAXS spectra with an analysis model, where details of the model analysis are given in SI and the obtained structure parameters are summarized in Table 1. The fitting parameters include the

Table 1. Structure Parameters Obtained by Fitting the Small Angle X-ray Scattering Data from Core-Shell NCs with Different Core Structures

NCs	*Rc* (Å)	T_S (Å)	$D_{NPs(avg)}$ (Å)	ALs	*P*
Pt NPs			30.6		0.05
Pt_s/Co_c	14.5	4.1	37.2	1.5	0.09
Pt_s/Ru_c	15.9	4.2	40.2	1.5	0.08

outer diameter $D_{NPs(avg)}$, the radii of core R_c, the thicknesses of shell T_s, and the polydispersity of the particle size *P*. There are two additional parameters, namely a fractal dimension D_F and a q-independent background (presented in SI). The numbers of Pt shell atomic layers (ALs) is given by $ALs = Ts/d_{(111)}$ (d(111) is the interplanar spacing of fcc (111) facet). Accordingly, the Pt_s/Ru_c comprises a 3.2 nm core and 1.5 atomic layer thick Pt shell. Similarly, the Pt_s/Co_c consists of a 2.9 nm core and a 1.4 atomic layer thick Pt shell. The growth of NCs with core−shell structure and precisely controlled shell thickness are evident since the polydispersity (*P*) of the particle size is quite small (~0.08 − 0.09) as determined from the SAXS analysis.

Effects of Core Crystallites on Crystal Structure and Lattice Strain in Shell Region of Core−Shell NCs. After having recognized the growth of core−shell NCs with similar thicknesses of shell crystal by SAXS, we can consider that the lattice strain within Pt shell crystal is mainly dominated by the lattice structure of core crystallites. The effects of core crystallites on the crystal structure and lattice strain of Pt shell are illustrated by XRD. Before the XRD measurements, the NPs were dispersed at the surface of the silicon wafer and were treated by the same thermal conditions with which they are treated for CV analysis. Figure 2 compares the XRD patterns of Pt NPs (Figure 2a), Pt_s/Co_c (Figure 2b), and Pt_s/Ru_c (Figure 2c). The corresponding structure parameters are summarized in Table 2. As can be seen, the diffraction peaks at 26.49° (P1) and 30.65° (P2) are indications for the metallic characters from (111) and (200) facets of Pt NPs with an average coherent length (D) of 8.2 nm according to the Debye−Scherrer equation. The Pt_s/Co_c NC is a three-phase coexisted system. As shown in Figure 2b, the diffraction peaks A, C, and E corresponds to the characteristic signals from the (111), (220), and (331) facets of Co_3O_4 phase with a D_{avg}

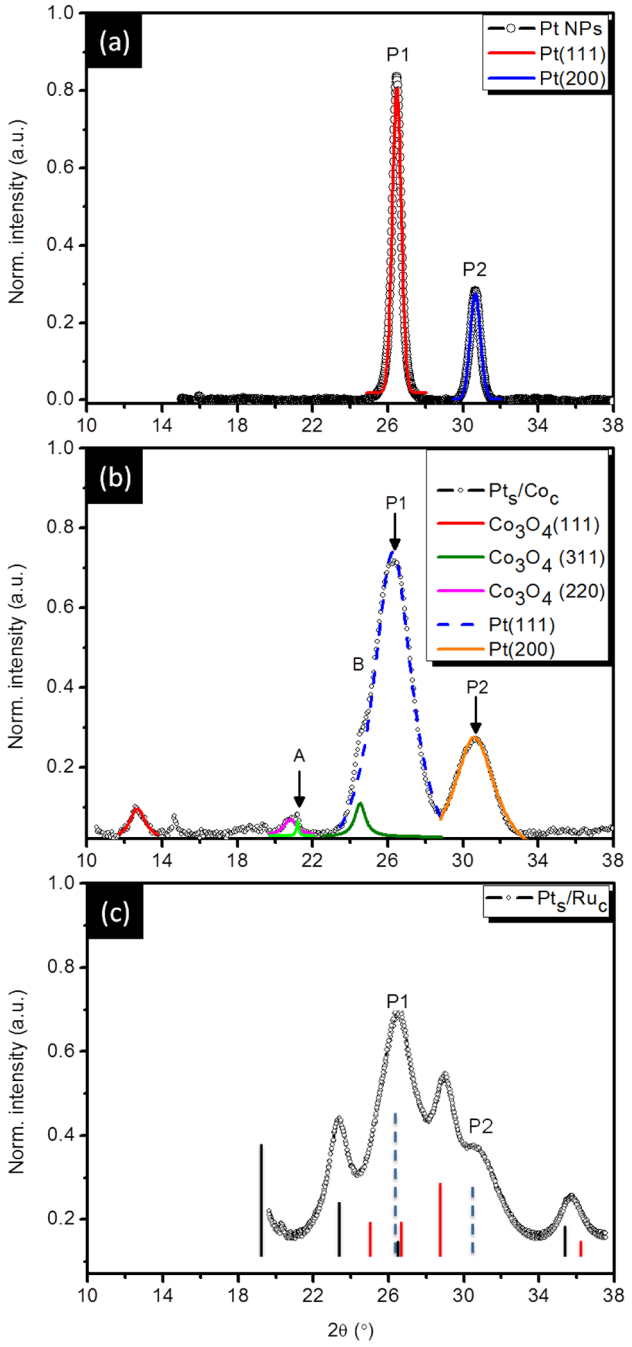

Figure 2. XRD patterns of Pt NPs (a), Pt_s/Co_c (2b), and Pt_s/Ru_c (c) with peak fitting curves. Red vertical lines represent the rutile RuO_2 phase (JCPDS file 88−0322), black vertical lines represent the hcp Ru phase (JCPDS file 88−1734), and blue dashed vertical lines represent the fcc Pt phase (JCPDS file 88−2343).

ranging from 59.3 to 70.8 Å. The peaks B and D could be attributed to the diffraction signals from cobalt carbide (CoC_8, Braga, D. et al. *J. Chem. Soc., Dalton Trans.* **1979**, 2026) with a D_{avg} of 314.2−378.1 Å. These giant carbide NPs might originated from the sintering of large polymer blended Co NPs retentions during the preparation of XRD samples. The broad peaks of P1 and P2 denote the formation of Pt fcc (111) and (200) facets with an estimated D_{avg} of 26−27 Å. There are three different types of crystallite phase that can be found in the Pt_s/Ru_c NCs. As shown in Figure 2c, the metallic Pt (111) and (200) characteristics peaks are denoted by the P1 and P2,

dx.doi.org/10.1021/jp3017419 | *J. Phys. Chem. C* 2012, 116, 16969−16978

Table 2. XRD Determined Structure Parameters of Bimetallic NPs

NCs	peak	index	$2\theta°$	$\Delta 2\theta°$	D (Å)	d (Å)
Pt NPs	P1	Pt (111)	26.47	0.57	123.87	2.25
	P2	Pt (200)	30.65	0.61	117.05	1.95
Pt_s/Co_c	A	Co_3O_4(111)	12.66	1.03	67.09	4.68
	B	CoC_8	14.67	0.22	314.23	4.05
	C	Co_3O_4(220)	20.94	1.18	59.38	2.84
	D	CoC_8 (008)	21.21	0.18	378.09	2.81
	E	Co_3O_4(331)	24.43	0.99	70.79	2.44
	P1	Pt(111)	26.28	2.55	27.66	2.27
	P2	Pt(200)	30.61	2.73	26.12	1.96
Pt_s/Ru_c	NA					

respectively. The peaks A and B coincide with the diffractions of the RuO_2 phase at (110) and (101) facets. Diffraction peaks of metallic Ru are also located in this region (denoted by the black vertical lines in Figure 3c), however, these signals are embedded under the strong reflections of Pt and RuO_2 phases. From results of SAXS we know that the $D_{NPs(avg)}$ of Pt_s/Ru_c is about ~4 nm (see Table 1) and the shell thickness is less than 0.5 nm. This information suggests that the corresponding full widths at half-maximum (fwhm, $\Delta 2\theta$) of each diffraction peak is larger than 1.6°. Therefore, it is inaccessible to extract the crystal structure parameters by deconvoluting the diffraction peaks in this region. To avoid the overlap issues, the crystal structure parameters were determined from peak C, where only the RuO_2 (211)/(121) would be observed. By adopting the peak feature, the position and peak width, the D_{avg} is determined to be 50.9 Å. Because a slight interparticle sintering is observed (see Figure 3c) between Pt_s/Ru_c NCs, the lattice modulation of the core−shell interface and restructure of Pt to Ru core is unavoidable and could be the possible reasons for the enlarged Pt D_{avg}.

The lattice strain of the Pt shell crystal, s(shell), in the two core−shell NCs is determined by the extent of their characteristic peaks offset from the peak of Pt NPs. With the careful background subtraction, the unexpected scattering interferences on the peak offset from the polymer retentions could be rule out from the spectra. Herein, the lattice strain in shell region could be estimated by eq 1:

$$s(\text{shell}) = \frac{a_{\text{shell}} - a_{\text{Pt}}}{a_{\text{Pt}}} \times 100 \quad (1)$$

where a_{Pt} is the bulk Pt lattice parameter (i.e., Pt NPs in our study). For Pt_s/Ru_c, the characteristic peaks of metallic Pt facets (P1 and P2) are found shifted to the high angle side from that of Pt NPs and has a lattice space determined to be 2.24 Å. It corresponds to a lattice constant of 3.87 Å that suggests that 0.7% of lattice compression from that of Pt NPs is due to the heterogeneous interface of Ru core crystallites. On the other hand, for Pt_s/Co_c, the P1 and P2 peaks shift to the lower angle side from that of Pt NPs and have the interplanar spacings of 2.27 and 1.96 Å, respectively. Accordingly, the Pt lattice constant in Pts/Coc could be determined to be 3.95 Å. Consequently, a 0.8% of lattice expansion was found. This could be attributed to the conjunction of Pt shell crystallite at a large lattice constant core crystallite (i.e., Co_3O_4 core crystallites 7.96 Å).

Effects of Core Crystallite on the Lattice Structure of Core−Shell NCs. The lattice structures of the three NCs are elucidated by using HRTEM. To obtain the consistent structure information, the samples were annealed with identical conditions to that of XRD and CV analyses. As shown in Figure 3a, the interplanar spacing of the Pt NPs is estimated to be 2.27 ± 0.01 Å, corresponding to that of Pt fcc (111) facet. Between Pt NPs, a severe interparticle sintering is found. This is because the reduction of surface Gibb's free energy by reducing the specific surface area of NPs that exposing to the environment. Figure 3b shows the HRTEM images for the Pt_s/Co_s. Clearly, the Pt_s/Co_c grows in isomeric symmetry without preferential facets. Such uniform shell growth is expected because the Co core crystal is well protected by capping polymers into a spherical particle without a specific facet (it a lattice space of 2.14 Å similar to that of the Co_2C "JCPDS no. 66−1457, see the inset). It has an average size of 3.5 nm and a crownlike

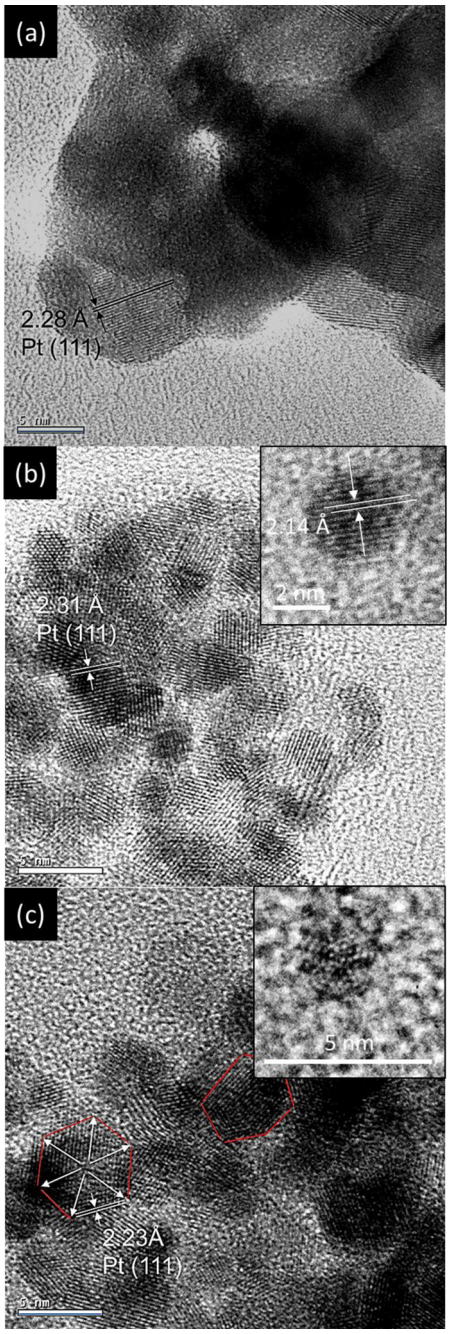

Figure 3. High resolution transmission electromicroscopy images of Pt NPs (a), Pt_s/Co_c (b), and Pt_s/Ru_c (c), respectively.

dx.doi.org/10.1021/jp3017419 | J. Phys. Chem. C 2012, 116, 16969−16978

surface. The interplanar spacing across the arrow direction is determined to be 2.31 ± 0.01 Å, corresponding to a Pt lattice constant of 4.01 ± 0.01 Å. This lattice constant is ~1.71% larger than that of f.c.c. Pt NPs (3.93 Å ± 0.01 Å), again suggesting an expansive lattice strain in Pt region of Pt_s/Co_c. The HRTEM image of Pt_s/Ru_c is shown in Figure 3c. It depicts the formation of thermodynamically and crystallographically stable particles because these particles are formed by growing Pt atoms at multifaceted polygons of Ru core crystal in the h.c.p. phase with the preferential facets at (101; 2.082 Å) and (002; 2.141 Å) (see inset of Figure 3c). From HRTEM image we can notice that the Pt_s/Ru_c grows into truncated hexoctahedral cone crystals (denoted by the arrows in images). The radiated aligned lattice plane (denoted by arrows) illustrates the preferential orientation growth of the Pt shell crystal at the thermodynamically stable {111} plane in a core-shell architecture. The lattice fringes of these particles are found to have an average interplanar spacing of 2.23 Å ± 0.01 Å, which is in agreement with that of Pt f.c.c. (111) facet. This value is slightly contracted from that of HRTEM determined Pt (111) facet (2.27 Å ± 0.01 Å), which consistently with the XRD results indicating a compressive lattice strain (−1.7%) in the Pt shell region.[6,9] In addition, a certain extent of interparticle sintering is found between the Pt_s/Ru_c NCs. This sintering is induced by the easy breaking of Ru−O−C bondings at particle surface[18] because a slight amount of Ru might segregate to particle surface upon preparing the NC samples for XRD and CV measurements by annealing.[9]

Atomic Structure, Electronic Structure, and the Corresponding Binding Energy of Shell Crystal in Core−Shell NCs. The core crystal structure also substantially affects the surface atomic structure, the unfilled d states, and the binding energies of the shell crystal. These characteristics, which could be deduced by using the X-ray absorption spectroscopy and the X-ray photoemission spectroscopy, illustrate from where the surface activity of the core−shell NCs are originated. Figure 4 compares the Pt L_3-edge XANES spectra of Pt NPs, different cored NCs, and Pt foil. The absorption features at 11564 eV corresponds to the electronic transitions of $2p_{3/2}$ to $5d_{3/2}$ of Pt metal; where the magnitude of the absorption hump and white-line[19] reflects the orbital occupancy of the 5d electronic state. Herein, it is expected to note that the white line intensity would increase with decreasing 5d orbital occupancy of Pt atoms. As can be seen, the white-line intensities for all samples are higher than that of a Pt foil. This could be caused by the charge donation from Pt to their neighboring atoms (i.e., oxygen in platinum oxide, cobalt in Co core, and ruthenium in Ru core).[20] The differences in the white-line intensity between the catalyst and a reference Pt foil were also quantified by a L-edges correlation that developed by Mansour et al.[19,21] To conduct the d-state quantification, the Pt L_2-edge XANES spectra of NCs are collected and are shown in Figure S1 (which showing the charge transition from $2p_{3/2}$ to $5d_{3/2}$). In this analysis, the fractional change in the total number of unfilled d states (f_d) of the NCs compared to the number of the reference foil can be formulated as eq 2:

$$f_d = \frac{\Delta A_3\sigma_3 + 1.11\Delta A_2\sigma_2}{A_{3r}\sigma_3 + 1.11A_{2r}\sigma_2} \quad (2)$$

After subtracting the Pt foil data from the NCs data, the resulting curves were then numerically integrated between −10 and 14 eV for both the L_2- and L_3-edges. The integrated areas (ΔA_2 at L_2-edge and ΔA_3 at L_3-edge, respectively) are normalized by multiplying with the X-ray absorption cross section at the edge jumps (σ). Upon data analysis, the absorption cross section at the Pt L_3- (σ_3) and L_2-edge (σ_2) were set to be 117.1 and 54.2 cm^{-2} g^{-1}, according to the standard database.[22] The values of A_{3r} and A_{2r} denote the integrated area of Pt foil at L_3 and L_2 edges, respectively. In addition, the number of unfilled d states in the sample (h_{Ts}) can then be represented by eq 3 if the number of unfilled d states in the reference material (h_{Tr}) is known:

$$h_{Ts} = (1 + f_d)h_{Tr} \quad (3)$$

Inset of Figure 4 demonstrates the calculated h_{Ts} of Pt in the core−shell NCs. This parameter relates to factors such as morphology, particle size, heteroatomic intermix, and the extent of oxidations of the NPs.[23] As shown, the h_{Ts} of Pt NPs is determined to be 1.64. Because the heteroatomic intermix is absence, the higher h_{Ts} of Pt NPs than Pt foil can be attributed to the particle size effect and to a certain extent of the surface oxidization. For Pt_s/Co_c, the smaller Pt domain size could be the main reason for the increased h_{Ts}. This is because the Pt shell atoms have a smaller coordination number (shown by the weaker radial peak intensity in Figure S2) and a similar extent of oxidation to that of Pt NPs (revealed by XPS in the following section). On the other hand, Pt_s/Ru_c has the highest h_{Ts}, which suggests its highest extent of valence charge donation from Pt to neighboring coordinates. This is possibly due to its smallest homotaomic coordination number of Pt domain (see Figure S2) and the largest extent of surface oxidation (or oxygen chemisorptions) and heterogeneous interface contact among the three NCs.[1,9]

The interatomic electronic interactions of core−shell NCs could be examined by using X-ray photoelectron spectroscopy (XPS) analysis. Figure 5 shows the background subtracted Pt 4f region of the spectra from the three NCs; where the fitting curves of the three valents Pt species with the background are given in Figure S3. Within this region, the two emission lines at ~73.5 and ~71.3 eV are originated from the contributions of the Pt $4f_{5/2}$ and $4f_{7/2}$ orbitals, respectively. In general, the probing depth of the emitted photoelectrons is about several nanometers (~3−10 nm) according to the Beer-Lambert relationships.[24] Because the sample thicknesses is far larger than the probing depth, the intensity of the emission peaks (denoted

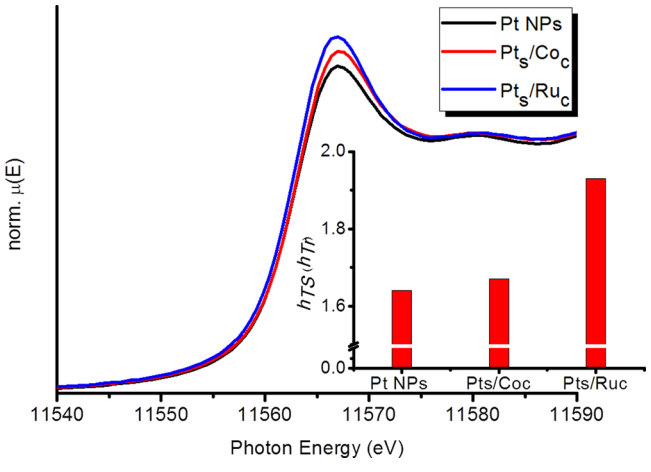

Figure 4. Pt L_3-edge XANES spectra of Pt NPs and core−shell NCs comprising Pt shell and different core crystallites.

dx.doi.org/10.1021/jp3017419 | J. Phys. Chem. C 2012, 116, 16969−16978

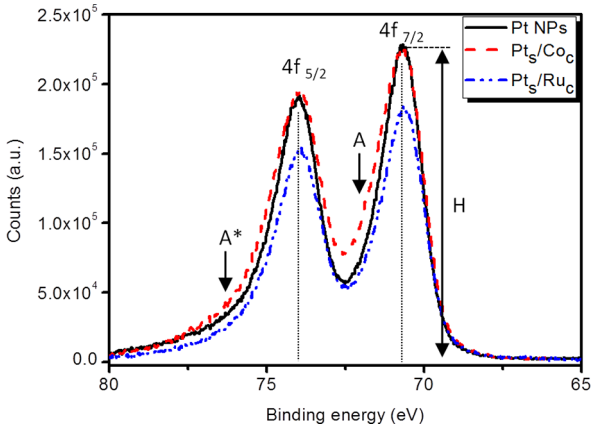

Figure 5. XPS spectra and their fitted components for the Pt 4f core levels of Pt NPs, Pt_s/Co_c, and Pt_s/Ru_c.

by H) could be considered as a qualitative index for the 4f electron density of Pt atoms. Therefore, the lowest H implies that the Pt_s/Ru_c has the lowest Pt 4f electron density among the three NCs. This implication is consistent with a lattice strain modified d-band model,[4,6] which reveals that the highest Pt unfilled d states (h_{Ts}, see inset of Figure 4) with the lowest H is the indication for a considerate amount of the Pt to neighboring charge donation due to a compressive lattice strain within the Pt_s/Ru_c shell region. Herein, with the stronger H and the smaller h_{Ts}, both the Pt NPs and Pt_sCo_c are expected to perform a lower extent of Pt charge donation to neighboring atoms compared to that of Pt_s/Ru_c. For Pt_s/Co_c, the shoulders appear (denoted by the arrows A and A*) at the high energy side of both the $4f_{5/2}$ and $4f_{7/2}$ emission peaks. This is obviously the single originated from the divalent Pt species with a positive offset of binding energy. Similarly, it could be explained by the d-band model with the expansive lattice strain in the Pt shell region.

The effects of core crystallite on the Pt valent distributions and the binding energy shifts are depicted by XPS analysis. For 4f region XPS of Pt NPs, the spectrum can be deconvoluted into three pairs of doublets. In each doublet, the BE of Pt $4f_{5/2}$ was about 3.33 eV higher than that of Pt $4f_{7/2}$. Among them, the most intense doublet (at 71.67 and 75.01 eV) is a signature of metallic Pt. The second and weaker doublet (at 72.84 and 76.16 eV) with BE at 1.22 eV higher than Pt(0) could be assigned to the Pt(II) valent state, which suggests the formation of species such as PtO and $Pt(OH)_2$.[25] The third doublet, which has the weakest in intensity and the highest BE (74.35 and 77.68 eV, as denoted by arrow A), is most likely caused by a small amount of Pt(IV) Pt precursors or PtO_2 oxide on NCs.[25,26] Table 3 summarizes the relative-area ratios of the integrated intensities (AR, surface compositions) of the three species for all of the NCs. As indicated, the zerovalent Pt metallic state is evidently predominated on the surface of the Pt NPs and Pt_s/Co_c (by ~68%). However, the Pt oxides (e.g., $Pt(OH)_2$, PtO, and Pt(IV)) prevail on the surface of Pt_s/Ru_c (by ~40%). The high surface Pt(IV) species ratio is possibly a consequence of the severe surface oxidation. According to fitting results, the metallic Pt doublet of core–shell NCs would shift to opposite sites from that of Pt NPs when their Pt atoms conjuncted to different types of core crystallites.

The BE shift is an indication for the charge translocation between Pt and neighboring atoms. It is a consequence of the heteroatom electronic interactions of Pt atoms including their

Table 3. Fitted XPS Surface Chemical Parameters (Binding Energies and Compositions) of Core–Shell NPs with Different Core Components[a]

NCs		Pt(0)	Pt(II)	Pt(IV)
Pt NPs	BE (eV)	71.67	72.84	74.35
	AR (%)	69.57	18.72	11.71
Pt_s/Co_c	BE (eV)	71.63	72.92	74.43
	AR (%)	68.57	17.28	14.15
Pt_s/Ru_c	BE (eV)	71.53	72.52	74.01
	AR (%)	62.19	27.60	10.21

[a]AR is the relative intensity ratio.

extent of alloying, their electronegativity difference to neighboring atoms, their surface oxidations distributions, and their lattice strain.[1,4,6] From XRD results we can notice that the Pt atoms experienced an expansive lattice strain of 0.7% in Pt_s/Co_c. Therefore, according to the theoretical d-band DFT predictions,[1,4,8] this lattice expansion is expected to see a substantial BE shift to high energy region in the 4f core level. However, the Pt BE of Pt_s/Co_c only slightly shifted by 0.1 eV compared to that of Pt NPs. This mild BE difference could be explained by the substantial charge back-donation (ligand effect) to Pt atoms because their electronegativity (2.28) is significantly higher than that of the core atoms (e.g., Co = 1.88). In addition, the Pt_s/Co_c has a similar extent of surface oxidation to that of Pt NPs (see Table 3). It implies that the surface oxidizes (including the oxygen chemisorptions and platinum oxide) should be ruled out from the interplay of Pt_s/Co_c BE shift in the Pt 4f region. On the other hand, compared to Pt NPs, the three Pt doublets of Pt_s/Ru_c are significantly shifted by −0.14 to −0.35 eV. This indicates a considerable amount of the charge donation from Pt to neighboring atoms as a result of the compressive lattice strain from the core crystal interface (Table 2).[4,8] In this case, the ligand effect between Pt and Ru is a minor factor in the BE shift because these two atoms have relatively compatible electronegativity (i.e., Pt = 2.28 and Ru = 2.2).

Electrochemical Performance of Core–Shell NCs. The MOR activity and durability of core–shell NCs are scrutinized by cyclic voltammetry (CV) and chronoamperometric (CA) measurements, respectively. The obtained anodic peak activity (I_F), activity at the half-peak potential at 0.5 V (I_{05}), electrochemical surface area (ECSA), and CO tolerance factor (I_F/I_B ratio, I_B denotes the cathodic peak activity) for all NCs are summarized in Table 4. Figure 6 compares the CV sweeping curves of experiment NCs with that of Pt NPs in a potential range from −300 to 1100 mV. When the potential is initially swept anodically a broad current peak coincides with the production of anodic charges was found. This anodic current is induced by the adsorption followed by the electrooxidation of MeOH at the surface Pt sites of NCs. It corresponds to the reaction of eq 4 (details of the MeOH electrooxidation pathways are shown in the eqs S1–S9 in SI):

$$CH_3OH + * \rightarrow 4H^+ + 4e^- + *\text{-}CO \quad (4)$$

where * denotes a Pt site on the surface of the nanocrystallites. The Pt site is poisoned by the intermediate product of CO (in a form of *-CO). Therefore, the desorption steps are necessary to regenerate the active site following the reaction in eq 5, [see also eqs S10–S13 in the SI for details].

$$*\text{-}CO + H_2O \rightarrow CO_2 + 2H^+ + * \quad (5)$$

dx.doi.org/10.1021/jp3017419 | J. Phys. Chem. C 2012, 116, 16969–16978

Table 4. Results of Cyclic Voltammetry of the Methanol Catalytic Oxidation and Hydrogen Reduction Activities of NCs[a]

NCs	V_{oc} (mV)	I_F (mA cm^{-2})	I_B (mA cm^{-2})	I_F/I_B	I_{500} (mA cm^{-2})	ECSA (before)	ECSA (after)
Pt NPs	150	2.71	2.91	0.93	0.85	24.71	28.02
Pt_s/Co_c	280	6.34	3.75	1.69	1.64	56.54	48.76
Pt_s/Ru_c	−135	3.18	0.605	5.25	2.95	125.61	109.36

[a]Two ECSA values are measured before and after MOR for 2 h.

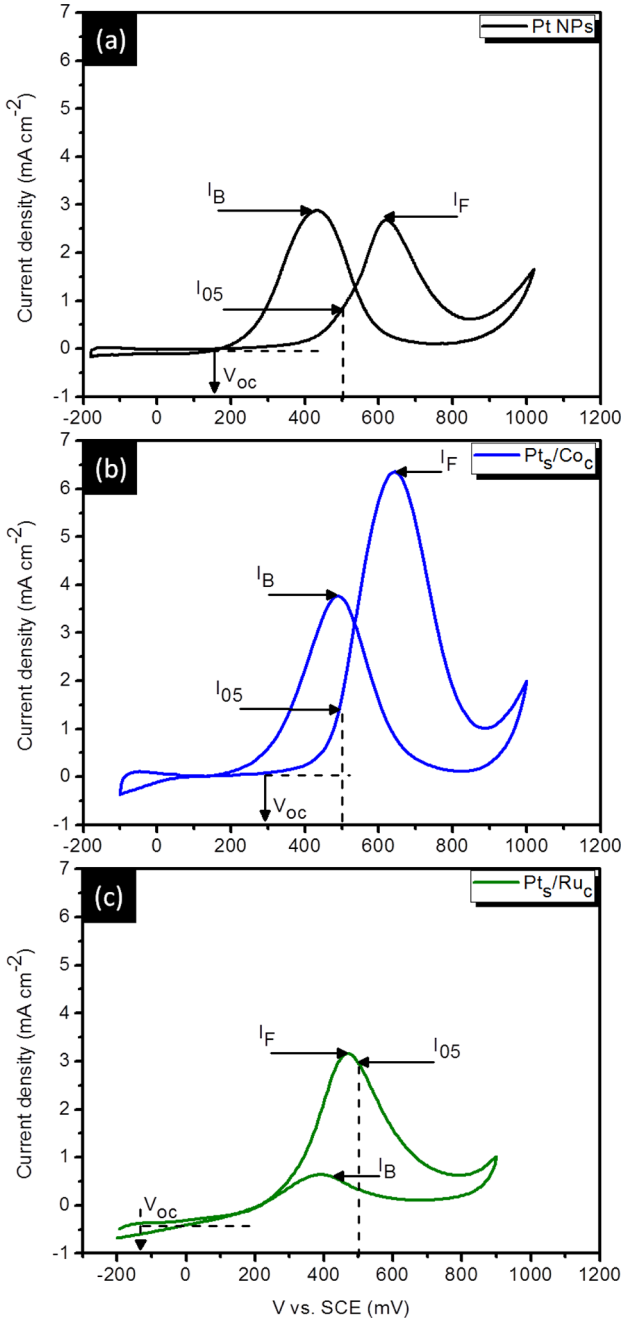

Figure 6. Cyclic voltametry sweeping curves of Pt NPs (a), Pt_s/Co_c (b), and Pt_s/Ru_c (c) on MeOH electrooxidation reactions.

Accordingly, a high performance NCs for MOR with low CO poisoning should give a high I_F accompanied with a suppressed cathodic I_B, therefore, performing a high I_F/I_B ratio.[27] Meanwhile, for catalysts with high electrochemical durability, a low current density degradation with a high ECSA is expected after a long-term MOR reaction. Most importantly, catalysts with a low onset potential (V_{oc}, which is the activation energy for catalysts to trigger MOR[28]) and a high density of valid Pt sites (N_{Pt}) are the essential criteria for developing the low temperature fuel cell system.[29] As observed from the CV results (Figure 6a), there are two oxidation reactions associated with Pt NPs that result in a positive current during the cathodic sweeping immediately after MeOH being oxidized: the oxidation potential of methanol (peak of I_F curve) is 625 mV defined as V_F and the oxidation potential of carbon monoxide is 430 mV defined as V_B. Upon potential sweep anodically, the oxidation current decreases sharply when the potential is higher than V_F. Such deactivation is induced by the formation of carbonaceous intermediates (e.g., aldehydes (−CHO^{ads}), carbonyl (−CO^{ads}), and carboxyl (−COOH^{ads})) at NPs surface that prevent the further adsorption and the subsequent oxidation of MeOH.[1,30,31] Peak electric current of CO oxidation (I_B) is 2.91 mA cm^{-2}, which is generated by the desorption of retained intermediates, is slightly higher than that of the MOR itself (i.e., I_F = 2.71 mA cm^{-2}). Accordingly, the I_F/I_B ratio of Pt NPs is determined to be 0.93, indicating that the CO poisoning effect is significant.[32] For Pt_s/Co_c, the I_F/I_B ratio is 82% higher than that of Pt NPs and the V_B becomes slightly electropositive (495 mV) (see Figure 6b and Table 4). The higher I_F/I_B ratio suggests the easier electrooxidation of carbonaceous intermediates for Pt_s/Co_c than Pt NPs. This could be attributed to a combination of bifunctional and ligand effects in a course of the slight surface Co segregation (as depicted by XPS and TPR analyses in Figure S3a and b, respectively). However, the high V_{oc} and V_B of Pt_s/Co_c refer to its high energy barrier for initiating the MOR and processing the CO electrooxidation reaction. On the contrary, the current density I_B for Pt_s/Ru_c has been substantially suppressed and the corresponding V_B becomes slightly electronegative (Figure 6c). Both the shifting of oxidation potential and the decreasing of current density depict the significantly weakened CO binding on the Pts/Ru_c compared to that on the rest of NCs. From the theoretical d-band model prediction and the XRD characterization results, such CO (or carbonaceous intermediates) bond weakening could be assigned to the contribution of compressive lattice strain in Pt shell crystal that exposing to a smaller lattice space surface (e.g., Ru core crystallites).

The column 6 in Table 4 compares the specific activity for all NCs at a potential of 500 mV (I_{500}, I at E = 500 mV). The variation of I_{500} can be attributed to a difference in the density of Pt sites (N_{Pt}) available on NCs in eq 6. Because all NCs were prepared by polyol reduction methods, it is expectable that a fraction of Pt atoms should have been occluded in core crystallite by the transmetalization followed by the self-restructure pathways.[9,33,34] As a result, the N_{Pt} available for the MOR increased not only with the dispersion of Pt atoms (D_{Pt}) on the catalyst, but also with the fraction of the Pt atoms exposed to the core surface (F_s).[35] Accordingly, the variation of I_{500} should be proportional to D_{Pt} and F_s, that is,

$$I_{500} \propto D_{Pt} \times F_s \quad (6)$$

dx.doi.org/10.1021/jp3017419 | J. Phys. Chem. C 2012, 116, 16969−16978

From geometry consideration, Pt NPs on the FTO electrode has an average size of $d_{Pt} \sim 13.4$ nm (see row 1 in Table 1), which corresponds to a dispersion of $D_{Pt} = 8.2\%$ by assuming that $D_{Pt} = 1.1/d_{Pt}$ (in nm).[35] Evidently, ~90% of the Pt atoms in Pt NPs do not participate in the surface reaction although the F_s is 100% (assuming that the Pt NPs is a core−shell structure with a topmost Pt layer that is located at a pure Pt core crystal). On the other hand, in core−shell NCs, 81.4% or higher ratio of Pt atoms would participate in the surface reaction, which is consistently illustrated by their substantial higher initial ECSA than Pt NPs as shown in the column 7 in Table 4.

The MOR durability of NCs is determined by chronoamperometric and the corresponding current-to-time curves are compared in Figure 7. Accordingly, the initial activity of Pt_s/Co_c is determined to be 1.69 mA cm^{-2}, which is 90% higher than that of Pt NPs (0.85 mA cm^{-2}). The long-term durability of both NCs was suppressed by ~60% after interacting with methanol for 20 min. Besides, regardless of the initial activity of Pt_s/Co_c and Pt NPs, the two catalysts cannot further interact with methanol after 60 min measurement. It is interesting to note that Pt_s/Ru_c has a 3.5-fold initial activity compared to that of Pt NPs. Meanwhile, it is the only catalyst that can generate a considerable high current density of 0.11 mA cm^{-2} after the long-term MOR measurement for 2 h. The ECSA of all NCs before and after the long-term MOR reaction are compared in Table 4 to clarify the origins of current degradation. Figure S4a, and S4b presents the CV curves of the three electrocatalysts without and with experiencing the long-term MOR at 0.5 V (vs SCE) for 2 h, respectively. For the catalysts without experiencing MOR, the reversible adsorption and desorption responses of hydrogen atoms are clearly found on the negative and positive sweeps, respectively. The electrochemical performances of NPs are mainly indexed by the ECSA and surface atomic configurations of Pt. The ECSA of all NPs can be determined by integrating the voltammetric current densities at potentials negative to about 0.36 V. This region is also called under-potential deposition hydrogen (UPD H) and its corresponding voltammetric charge is determined according to eq 7.[36,37]

$$\mathrm{PtECSA}[m^2\ g^{-1}] = \frac{(Q_{H\text{-}des}[C]) \times 100}{210\ \mu C\ cm^{-2} \cdot (w_{Pt}[g])} \quad (7)$$

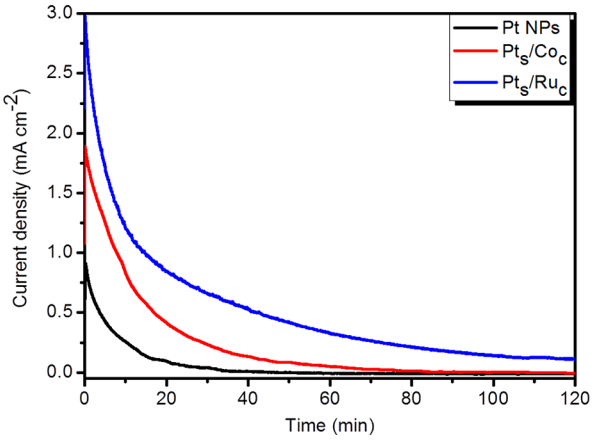

Figure 7. Long-term MOR current-to-time chronoamperometric curves of three NCs.

where $Q_{H\text{-}des}$ refers to the voltammetric charge density resulting from H desorption; meanwhile, 210 $\mu C\ cm^{-2}$ is the standard hydrogen desorption charge (a factor) corresponding to unit surface area of Pt. Under the same loading of Pt, different UPD H peaks are observed for NCs in varies structures. This represents the different surface areas of the three catalysts (see Table 4). As can be seen, the ECSA of Pt NPs is increased by 13.47% after the 2 h MOR. It shows that the Pt-skin structure might have collapsed to generate a new surface area as a result of the effect of chemical etching. For the same reason, the ECSA of Pt_s/Ru_c and Pt_s/Co_c were decreased by ~13−14%. This is because a certain amount of the NCs were detached from the FTO surface.[5] Therefore, the similarities of ECSA suggest that the significant current decay is a combination result mainly by the sorption of carbonaceous intermediates at surface active sites (Pt) and partially by the loss of NCs from the FTO substrate. For the case of Pt_s/Co_c, a significant change in the feature of anodic sweeping region, suggesting a dramatic adsorbate-induced restructuring and the acidic etching of their surface adatoms after the 2 h MOR (see Figure S4).[5,38] However, for Pt_s/Ru_c, such surface modification is nearly absent, indicating its strongest chemical durability among the presenting NCs.

Taking results from the X-ray analysis (XAS, XPS, XRD, and SAXS) and electrochemical analyses together, a plausible pathway explaining the current decay of NCs with atomic structure evolutions for a long-term MOR is proposed and is shown in Figure 8. It shows how the surface morphology of NCs evolves from a core−shell structure upon interacting with the methanol in the presence of hydrogen anions. Accordingly, the damage of the surface Pt layer is unavoidable upon the interaction between NCs and methanol for a long-term measurement. It would result in different consequences on the performance of NCs. For instance, H^+ corrosion would remove the outmost Pt skin to reduce the particle size of Pt NPs and consequently increase the specific ECSA of the electrode. On the other hand, it disconnects the core−shell NCs, therefore, reducing the ECSA of experimental electrodes. We believe that during the MOR process the electrolyte would

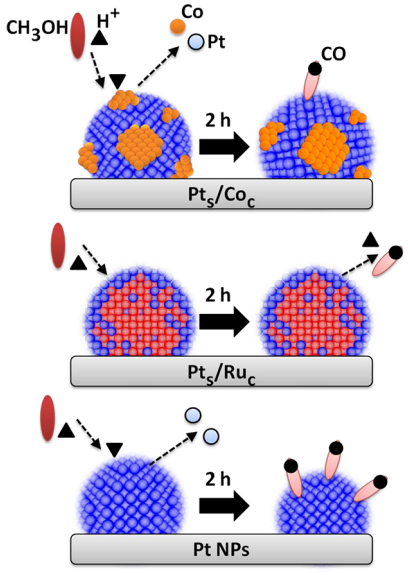

Figure 8. Proposed structure evolution of NCs after MOR for 2 h, deduced from X-ray and electrochemical measurements.

dx.doi.org/10.1021/jp3017419 | J. Phys. Chem. C 2012, 116, 16969−16978

pass through the imperfect Pt skin into embedded layers underneath and, consequently, dissolves the cobalt core. This phenomenon finally causes the collapse and restructuring of the imperfect Pt skin into Pt clusters, therefore, rendering the surface activities of catalysts. Proper annealing and synthetic processes enable the modification of the imperfect Pt skin, which may improve the catalytic activity and stability.[5,10,39] Our findings demonstrate the importance of appropriate synthesis sequences and the method could be applied to other Pt bimetallic alloys also associated with transition metals. In this work, we found that the Pt_s/Co_c NCs initially comprises an ~2.3 nm Co core and 1.5−1.7 atomic layers thick Pt shell crystal. After an annealing treatment, the Co atoms would mainly be oxidized into Co_3O_4 and partially be segregated to the surface. This oxidation may result in a rough and uncompleted Pt skin with sculpted shapes (see HRTEM images in Figure 3) and thus induces a slight extent of heteroatomic Pt-to-Co conjunctions at particle surface. Similarly, parts of Ru atoms in Pt_s/Ru_c NCs might segregate to the surface after annealing. However, their core region consists of metallic Ru and RuO_2 crystallites that have a smaller lattice constant than Pt shell. This lattice difference would build a compressive lattice strain to reinforce the Pt shell atoms and thus to promote the surface activity of NCs. It is such a difference of core crystallites that can be applied to modulate the lattice strain in the Pt region and thus to manipulate the surface activity of NCs.

CONCLUSION

Two types of core−shell NCs were synthesized by the polyol reduction method with sequential control in order to study how their surface activities over MOR had been engineered upon varying the structure of core crystallites. In Pt_s/Co_c, the large lattice space core would expand the interatomic distance between Pt atoms, thus, raising the energy barrier (onset potential) for MOR. The partial surface segregation of Co would participate as ligand pairs of surface Pt sites that slightly improving the CO tolerance of Pt_s/Co_c (I_F/I_B ratio) compared to that of Pt NPs. When the methanol electrooxidation process was carried out for 2 h, the electrolyte penetrated through the imperfect Pt skin and dissolved the cobalt atoms presented in layers underneath and on the outmost surface. Then the surface feature collapsed, thus, drastically suppressing the methanol oxidation activity of NCs. For Pt_s/Ru_c, the compressive strain from a small lattice core diminishes the energy barrier of Pt sites for the MOR. It weakens the bonding of surface carbonaceous intermediates, therefore, substantially improving the CO-tolerance of Pt_s/Ru_c. In addition to the prevention of surface poisoning, the Ru core would also protect the surface Pt atoms from corrosion, hence, prolonging the lifetime of NCs for MOR. Our findings demonstrate that, by the proper synthetic methods on controlling the atomic architecture of core−shell catalysts, the activities of NCs can be significantly enhanced. We believe that this method can also be extended to other Pt bimetallic alloys with transition metals to significantly improve their performance of MOR.

ASSOCIATED CONTENT

Supporting Information

The SAXS model derivation, data collection, and data analysis. The Fourier transformed extended X-ray absorption spectra, the X-ray photoemission spectra, and the temperature-programmed reduction spectra of the three types of NCs. The CV curves for measuring the ECSA of the three NCs and the details of methanol electrooxidation reaction steps. This material is available free of charge via the Internet at http://pubs.acs.org.

AUTHOR INFORMATION

Corresponding Author

*E-mail: chencaeser@gmail.com. Tel.: +886-3-5742671. Fax: +886-3-5728445.

Notes

The authors declare no competing financial interest.

ACKNOWLEDGMENTS

The authors would like to thank the staff of National Synchrotron Radiation Research Center (NSRRC), Hsinchu, Taiwan, for the help in various synchrotron-based measurements techniques. A special thank you is due to Prof. Shih-Yuan Lu and his research group (Dept. of Chemical Engineering, NTHU) who helped to analyze the CV data. T.-L.L. acknowledges the financial support received from National Science Council and Atomic Energy Council mutual fund (NSC 96-2623-7-007-022-NU and NSC 97-2623-7-007-006-NU).

REFERENCES

(1) Adzic, R. R.; Zhang, J.; Sasaki, K.; Vukmirovic, M. B.; Shao, M.; Wang, J. X.; Nilekar, A. U.; Mavrikakis, M.; Valerio, J. A.; Uribe, F. *Top. Catal.* **2007**, *46*, 249−262.
(2) Besenbacher, F.; Chorkendorff, I.; Clausen, B. S.; Hammer, B.; Molenbroek, A. M.; Nørskov, J. K.; Stensgaard, I. *Science* **1998**, *279*, 1913−1915.
(3) Hogarth, M. P.; Ralph, T. R. *Platinum Met. Rev.* **2002**, *46* (4), 117−135.
(4) Schlapka, A.; Lischka, M.; Gross, A.; Kasberger, U.; Jakob, P. *Phys. Rev. Lett.* **2003**, *91*, 016101.
(5) Sasaki, K.; Naohara, H.; Cai, Y.; Chio, Y. M.; Liu, P.; Vukmirovic, M. B.; Wang, J. X.; Adzic, R. R. *Angew. Chem., Int. Ed.* **2010**, *49*, 8602−8607.
(6) Alayoglu, S.; Nilekar, A. U.; Mavrikakis, M.; Eichhorn, B. *Nat. Mater.* **2008**, *7*, 333−338.
(7) Alayoglu, S.; Eichhorn, B. *J. Am. Chem. Soc.* **2008**, *130*, 17479−17486.
(8) Bligaard, T.; Nørskov, J. K. *Electrochim. Acta* **2007**, *52*, 5512−5516.
(9) Chen, T.-Y.; Lin, T.-L.; Luo, T.-J. M.; Chio, Y.; Lee, J.-F. *ChemPhysChem* **2010**, *11* (11), 2383−2392.
(10) Huang, S.-Y.; Chang, S. M.; Lin, C. L.; Chen, C. H.; Yeh, C.-T. *J. Phys. Chem. B* **2006**, *110*, 23300−23305.
(11) Guo, Y.-G.; Hu, J.-S.; Zhang, H.-M.; Liang, H.-P.; Wan, L.-J.; Bai, C.-L. *Adv. Mater.* **2005**, *17*, 746−750.
(12) Watanabe, M.; Motoo, S. *J. Electroanal. Chem.* **1975**, *60*, 275−283.
(13) Strasser, P.; Koh, S.; Anniyev, T.; Greeley, J.; More, K.; Yu, C.; Liu, Z.; Kaya, S.; Nordlund, D.; Ogasawara, H.; Toney, M. F.; Nilsson, A. *Nat. Chem.* **2010**, *2*, 454−460.
(14) Zhang, J.; Lima, F. H. B.; Shao, M. H.; Sasaki, K.; Wang, J. X.; Hanson, J.; Adzic, R. R. *J. Phys. Chem. B* **2005**, *109* (48), 22701−22704.
(15) Lin, J.-M.; Lin, T.-L.; Jeng, U.-S.; Zhong, Y.-J.; Yeh, C.-T.; Chen, T.-Y. *J. Appl. Crystallogr.* **2007**, *40*, s540−s543.
(16) Teixeira, J. *J. Appl. Crystallogr.* **1988**, *21*, 781−785.
(17) Wagner, J. *J. Appl. Crystallogr.* **2004**, *37*, 750−756.
(18) Wu, Z.; Wang, D.; Ren, W.; Zhao, J.; Zhou, G.; Li, F.; Cheng, H. *Adv. Funct. Mater.* **2010**, *20*, 3595−3602.
(19) Reifsnyder, S. N.; Otten, M. M.; Sayers, D. E.; Lamb, H. H. *J. Phys. Chem. B* **1997**, *101*, 4972−4977.

(20) Roth, C.; Benker, N.; Buhrmester, T.; Mazurek, M.; Loster, M.; Fuess, H.; Koningsberger, D. C.; Ramaker, D. E. *J. Am. Chem. Soc.* **2005**, *127*, 14607−14615.
(21) Mansour, A. N.; Cook, J. W.; Sayers, D. E. *Chem. Phys.* **1984**, *88*, 2330.
(22) McMaster, W. H.; Grande, N. K. D.; Hubell, J. H.; Mallett, J. H. *Compilation of X-ray Cross Sections*; National Technical Information Service: Springfield, 1969.
(23) Hwang, B. J.; Kumar, S. M. S.; Chen, C. H.; Chang, R. W.; Liu, D. G.; Lee, J. F. *J. Phys. Chem. C* **2008**, *112*, 2370.
(24) Watts, J. F.; Wolstenholme, J. *An Introduction to Surface Analysis by XPS and AES*; John Wiley and Sons, Ltd.: West Sussex, England, 2003.
(25) Liu, Z.; Lee, J. Y.; Chen, W.; Han, M.; Gan, L. *Langmuir* **2004**, *20*, 181−187.
(26) Liu, F.; Lee, J. Y.; Zhou, W. J. *Small* **2006**, *2*, 121−128.
(27) Burstein, G. T.; Barnett, C. J.; Kucernak, A. R.; Williams, F. R. *Catalyst Today* **1997**, *38*, 425−437.
(28) Geng, D.; Lu, G. *J. Phys. Chem. C* **2007**, *111*, 11897−11902.
(29) Huang, S.-Y.; Chang, C.-M.; Yeh, C.-T. *J. Catal.* **2006**, *241*, 400−406.
(30) Cohen, J. L.; Volpe, D. J.; Abruna, H. D. *Phys. Chem. Chem. Phys.* **2007**, *9*, 49−77.
(31) Newson, J. D.; Riddiford, A. C. *J. Electrochem. Soc.* **1961**, *108*, 699−706.
(32) Watanabe, M.; Uchida, M.; Motoo, S. *J. Electroanal. Chem.* **1987**, *229*, 395−406.
(33) Sun, Y.; Xia, Y. *Science* **2002**, *298*, 2176−2179.
(34) Sun, Y.; Yin, Y.; Mayers, B. T.; Herricks, T.; Xia, Y. *Chem. Mater.* **2002**, *14*, 4736−4745.
(35) Garcia-Cortes, J. M.; Perez-Ramirez, J.; Illan-Gomez, M. J.; Salinas-Martinez de Lecea, C. *Catal. Commun.* **2003**, *4*, 165.
(36) Hu, C.-C.; Liu, K.-Y. *Electrochim. Acta* **1999**, *44*, 2727−2738.
(37) Hu, C.-C.; Liu, K.-Y. *Electrochim. Acta* **2000**, *45*, 3063−3068.
(38) Mayrhofer, K. J.; Juhart, V.; Hartl, K.; Hanzlik, M.; Arenz, M. *Angew. Chem., Int. Ed.* **2009**, *48* (19), 3529−3531.
(39) Huang, S.-Y.; Chang, C. M.; Wang, K. W.; Yeh, C.-T. *ChemPhysChem* **2007**, *8*, 1774−1777.